Determination of Thermodynamic Cloud Phase and Reflective Field from Radiance Measurements

J. Um and G.M. McFarquhar
Department of Atmospheric Sciences
University of Illinois at Urbana-Champaign
Urbana, Illinois

Introduction

The thermodynamic cloud phase and composition have substantial impacts on vertical profiles of radiative heating. However, reliable retrievals of these quantities from remote sensing measurements are still difficult. Furthermore, retrieval techniques using satellite radiance measurements are limited to at most a few viewing angles. During the 2004 Mixed-Phase Arctic Clouds Experiment (M-PACE) at the North Slope of Alaska site, the Diffuse Field Camera (DFC) was mounted on the Proteus aircraft and measured cloud radiance fields in an effort to retrieve information about thermodynamic phase and dominant crystal habit. In this study, cloud radiance fields measured by Atmospheric Radiation Measurement Program Uninhabited Aerospace Vehicle's (UAV's) DFC are used to derive the complete directional dependence of cloud reflectance, which is related to cloud phase and composition, and then compared with calculated reflectance fields of water and ice clouds.

Diffuse Field Camera

The DFC was developed by the Marine Physical Laboratory, a component of the Scripps Institution of Oceanography, and has the primary purpose of measuring the directional variance of the upwelling radiation field. The DFC consists of a pair of nadir-mounted digital cameras with hemispheric field-of-view lenses with one visible (VIS) and one near-infrared (NIR) pass filter. Figure 1 shows the payload pod in which DFC was mounted and the DFC mounted inside the payload pod behind transparent domes. Detailed operating characteristics of the DFC are summarized in Table 1.

Figure 1. ARM UAV Proteus. The payload pod in which the DFC is mounted was indicated by the red arrow in the upper panel. Diffuse Field Cameras (blue arrows) mounted inside the payload pod behind transparent domes view in the nadir hemisphere.

| **Table 1**. Operating characteristics of the DFC		
	VIS	**NIR**
Pass filter (nm)	620 – 670	1580 – 1640
Pixel array	1300 × 1030	320 × 256
Viewing solid angle resolution (μsr)	~ 8	~ 130
Viewing direction	Nadir	Nadir

2004 M-PACE Observations

Twelve DFC NIR scenes with horizontally homogeneous boundary layer stratus (Figure 2) from the 12 October 2004 M-PACE flight of the Proteus were selected for analysis (Figure 3). Scenes from this experiment with relatively homogeneous clouds were analyzed to reduce complications from three-dimensional cloud radiative effects. The clouds had tops dominated by water with precipitating ice below (McFarquhar et al. 2005). Figure 4 shows an example of a DFC NIR scene from 12 October 2004. The viewing zenith angle and relative azimuth angle, which is measured from the Sun to the viewing direction clockwise, are indicated by red and black, respectively.
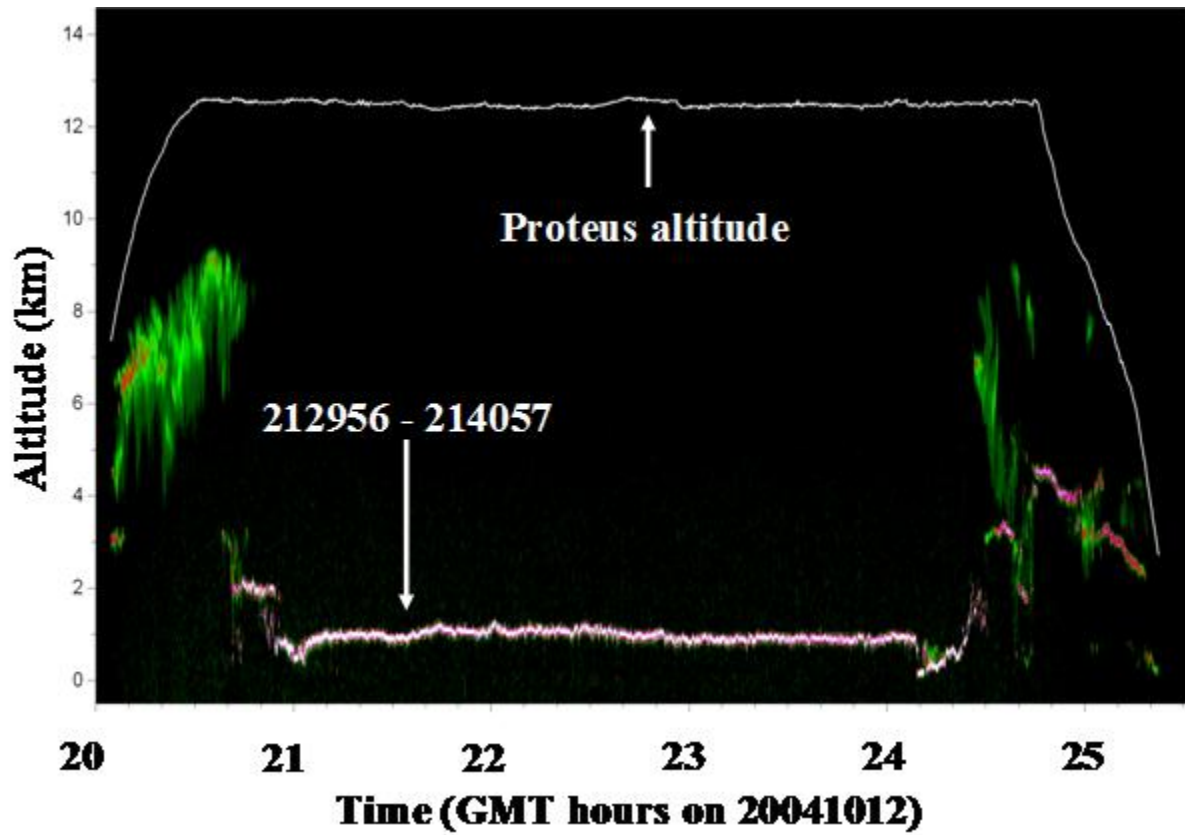
Figure 2. Normalized backscatter intensity measured by the Cloud Detection Lidar on 12 October 2004. The time period for the 12 selected scenes and the Proteus altitude are indicated.
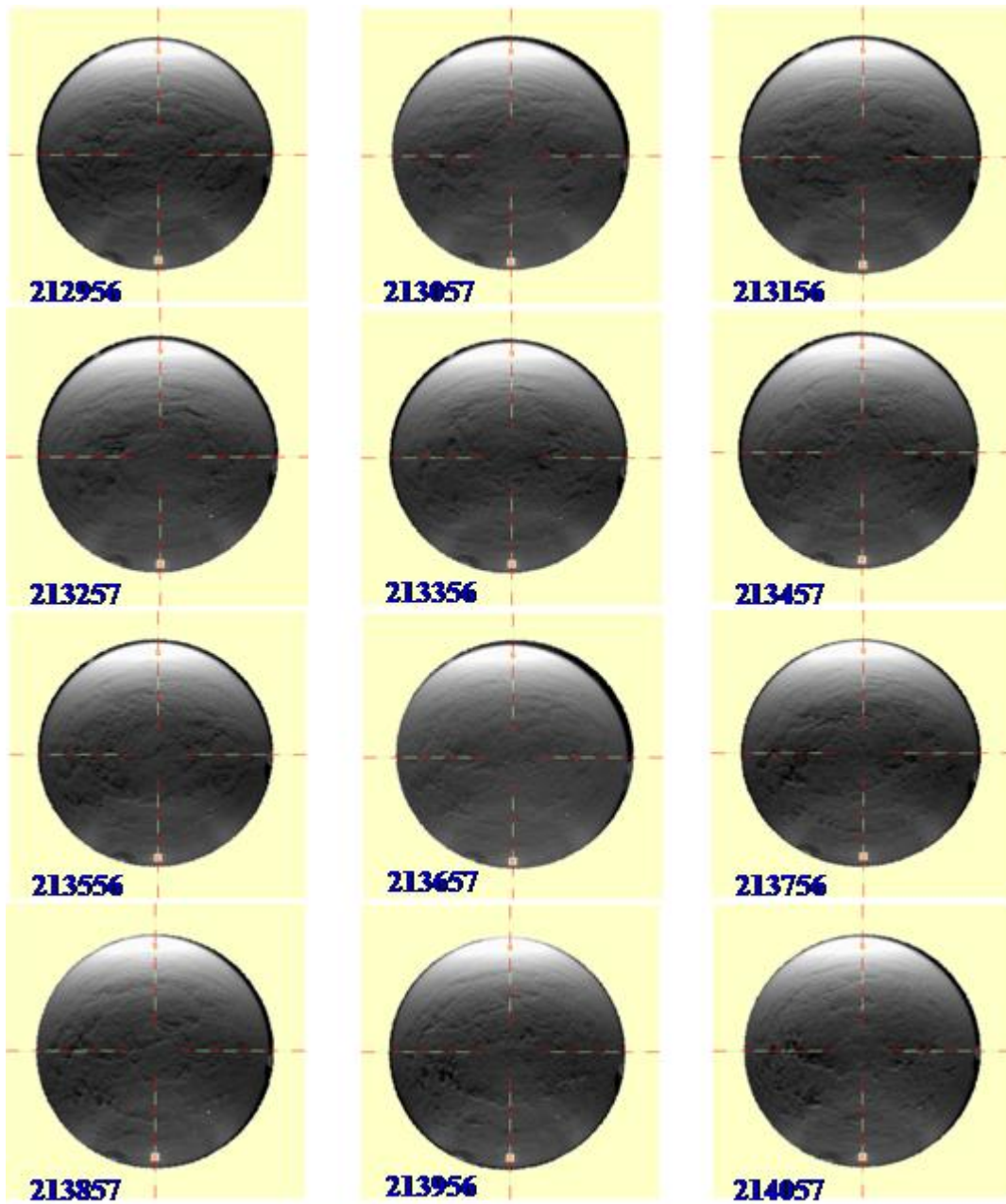
Figure 3. Twelve selected scenes of DFC NIR from 12 October 2004. Corresponding times are indicated in each scene.
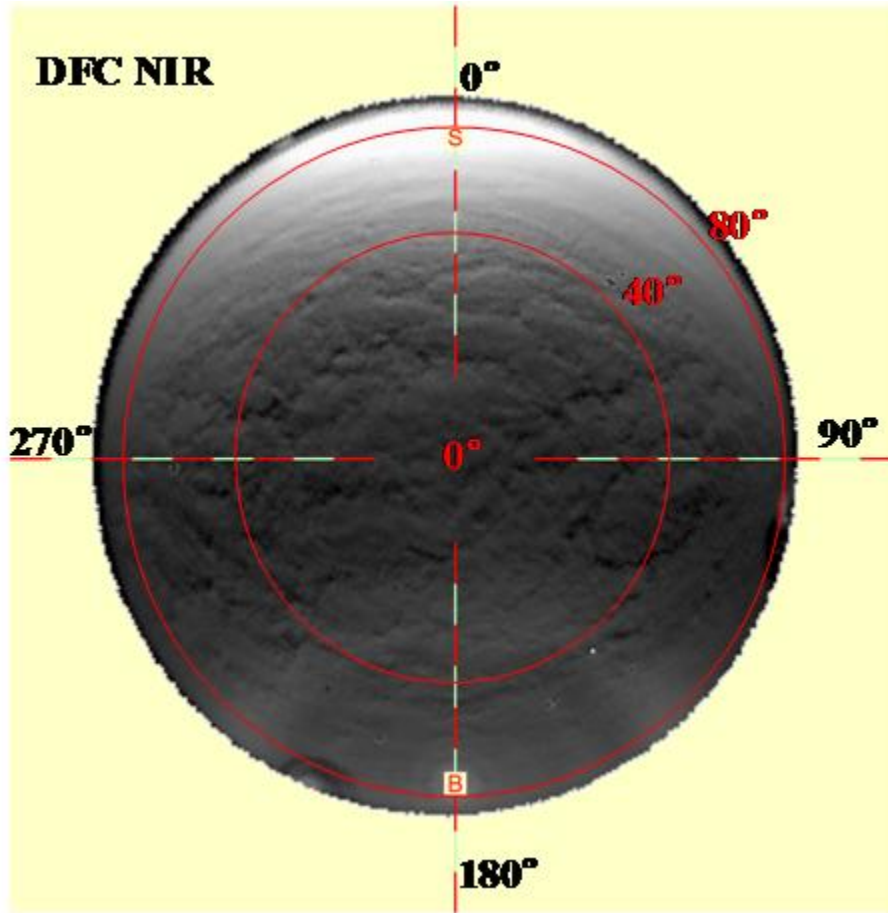
Figure 4. Example of DFC scene from 12 October 2004 at 212956 Universal Time Coordinates. Viewing zenith and relative azimuth angles are indicated by red and black, respectively. The letters S and B indicate the direction of the Sun and backscattering, respectively.

The 12 selected radiance fields (L_{mea}) measured by the DFC NIR were averaged and converted to a reflectance function (R) by

$$R = \frac{\pi L_{mea}}{\cos \theta_S F},$$

(1)

where ? θ_s is the solar zenith angle and F is the solar irradiance. Figure 5 shows how the directional dependence of reflectance is calculated given the sun position and relative position of Proteus. Given the sun position (S) and viewing vector (V) the scattering angle (Θ_{sca}) is calculated by

$$\Theta_{sca} = \cos^{-1}\left(\frac{S \circ V}{|S||V|}\right) = \cos^{-1}\left(\sin \theta_S \cos \varphi_V \sin \theta_V - \cos \theta_S \cos \theta_V\right)$$

,

(2)

where θ_v and φ_v are the viewing zenith and relative azimuth angle, respectively. Here, the azimuth angle of the Sun is always zero.
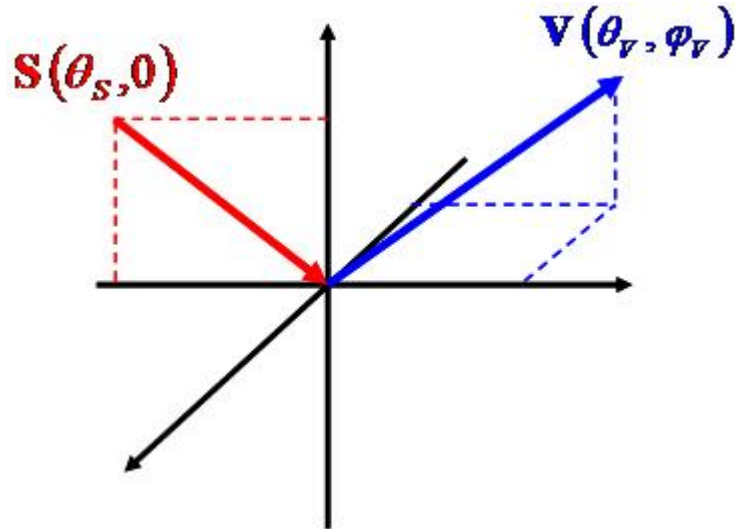

Figure 5. Unit vectors denoting the Sun position (red) and viewing direction (blue). A relative azimuthal angle is measured from the Sun to the viewing direction clockwise. Each unit vector is characterized by a zenith (θ) and azimuthal angle (φ). The Sun azimuthal angle is always zero.

Results

Observation

Using the 12 selected DFC NIR scenes, the directional dependence of the mean reflectance field was calculated. Figure 6 shows the mean reflectance function of the 12 selected DFC NIR scenes as a function of the view zenith and relative azimuth angle (left) and as a function of scattering angle (right) derived using Eq. (2). The red line in the right panel is the reflectance function averaged every degree. Strong backscattering (blue arrow) and a 140° peak (red arrow) can be seen. Although the strong backscattering can be found in both water and ice cloud reflectance fields, the 140° peak is an intrinsic feature of only water clouds (i.e., primary rainbow angle). Featureless lateral scattering and strong forward scattering are also noted in Figure 6.
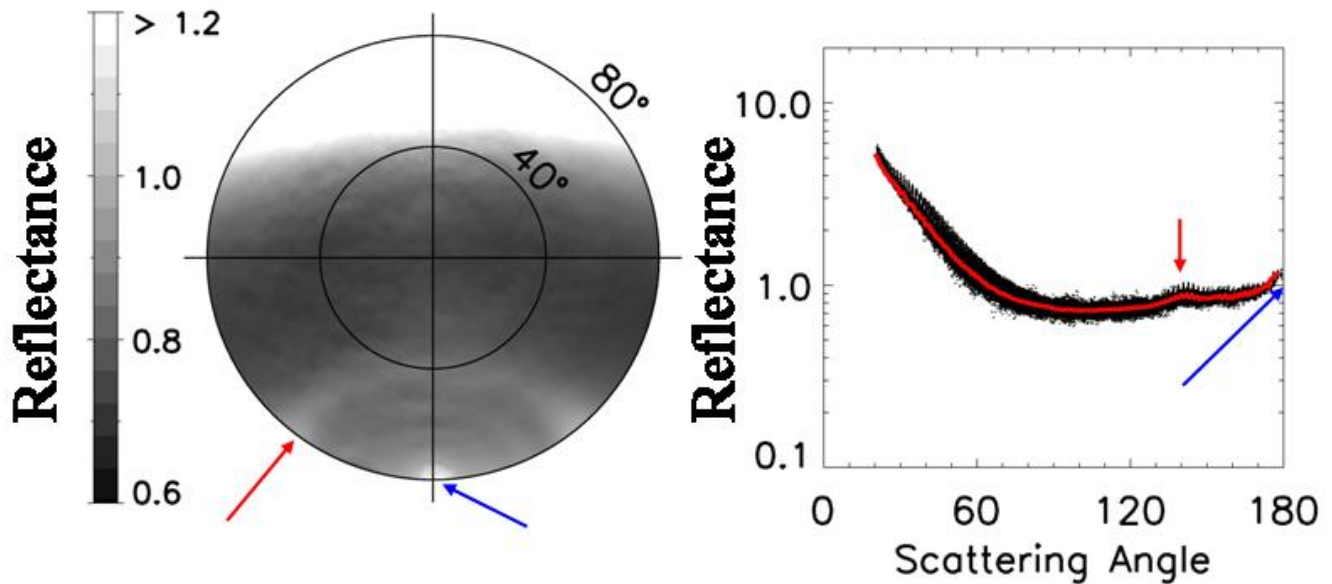
Figure 6. Mean reflectance fields from 12 selected scenes (left) and refigured mean reflectance fields as a function of scattering angle (right).

Theoretical Calculations

To compare observations shown in Figure 6 with theoretical calculations, the scattering phase function of water droplets with an effective radius of 12 μm were computed using Mie theory and that of aggregates of bullet rosettes (ABRs, Um and McFarquhar 2006) using geometric ray tracing The calculations are shown in Figure 7. ABRs were assumed to be clusters of six different bullet rosettes. The reflectance functions of water and ice clouds were then calculated using a Monte Carlo radiative transfer code developed by Macke at al. (1995) and the scattering phase functions shown in Figure 7. An optical depth of 30 was assumed for both water and ice clouds consistent with estimates made from radiometric observations during M-PACE (Mather, personal communication 2006). An average solar zenith angle of 78.98° from the 12 selected DFC scenes was used in these calculations.
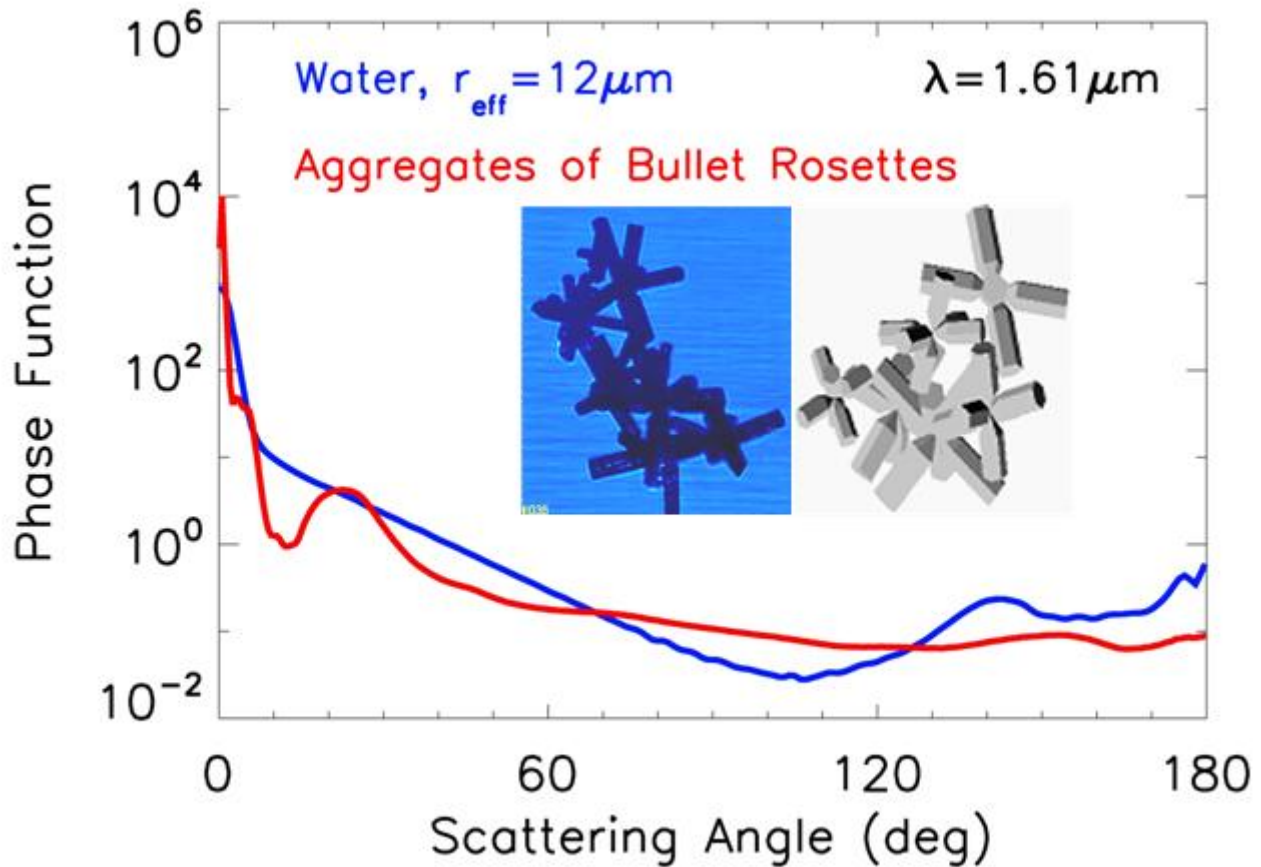
Figure 7. Theoretical scattering phase functions for water droplets computed by Mie theory and for aggregates of bullet rosettes (ABRs) with rough surface computed by geometric optics. A CPI image (blue background) and idealized model of ABRs are embedded in the figure.

Figures 8 and 9 show the reflectance fields of water and ice clouds calculated using the technique described above. Water clouds show strong backscattering and a 140° peak or cloudbow in the calculated reflectance fields, whereas ice clouds reveal relatively weak backscattering and a 150° peak. Furthermore, the reflectance fields of ice clouds are broader than those of water clouds. This occurs because absorption due to ice is more effective than absorption due to water at this wavelength (i.e., 1.61 μm); the single scattering albedos of ABRs and of water droplet at this wavelength are 0.89 and 0.99, respectively. The mean reflectance function of the DFC NIR and the theoretically calculated mean reflectance function of water and ice clouds are compared in Figure 10. The calculated reflectance function of water cloud shows good agreement with that of DFC NIR in the backscattering region and captures the 140° cloudbow feature even though there is a difference in the absolute value of the reflectance function. On the other hand, ice clouds reveal larger differences in the lateral and backscattering regions compared to the observations. The closer match of the observed reflectance function to that of water clouds is consistent with the in-situ observations that showed the mass and radiative properties of these M-PACE boundary layer clouds were dominated by the water droplets.
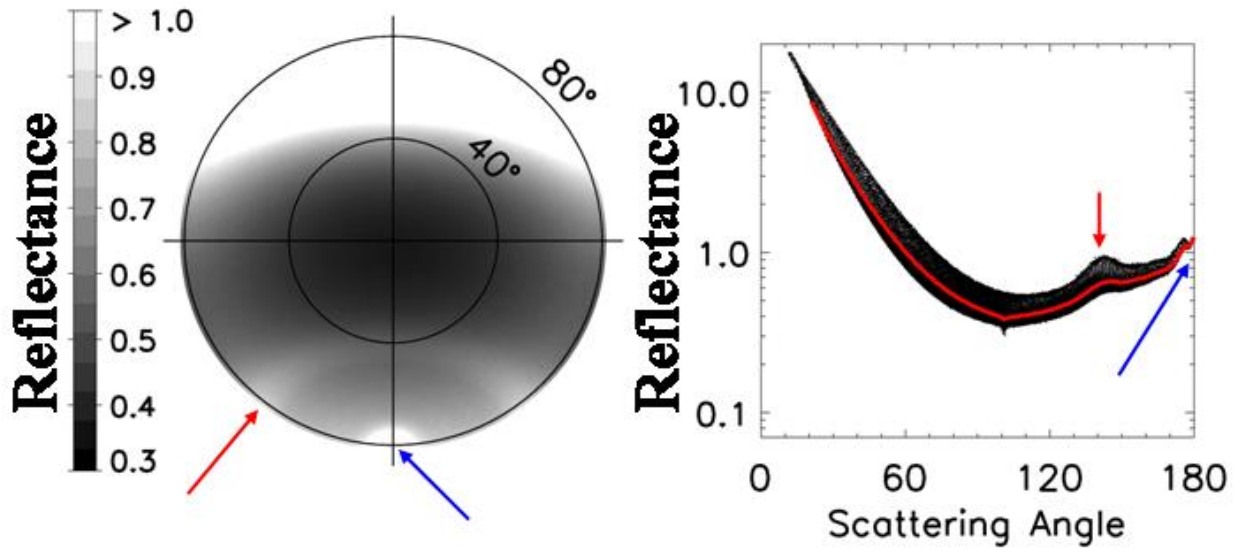
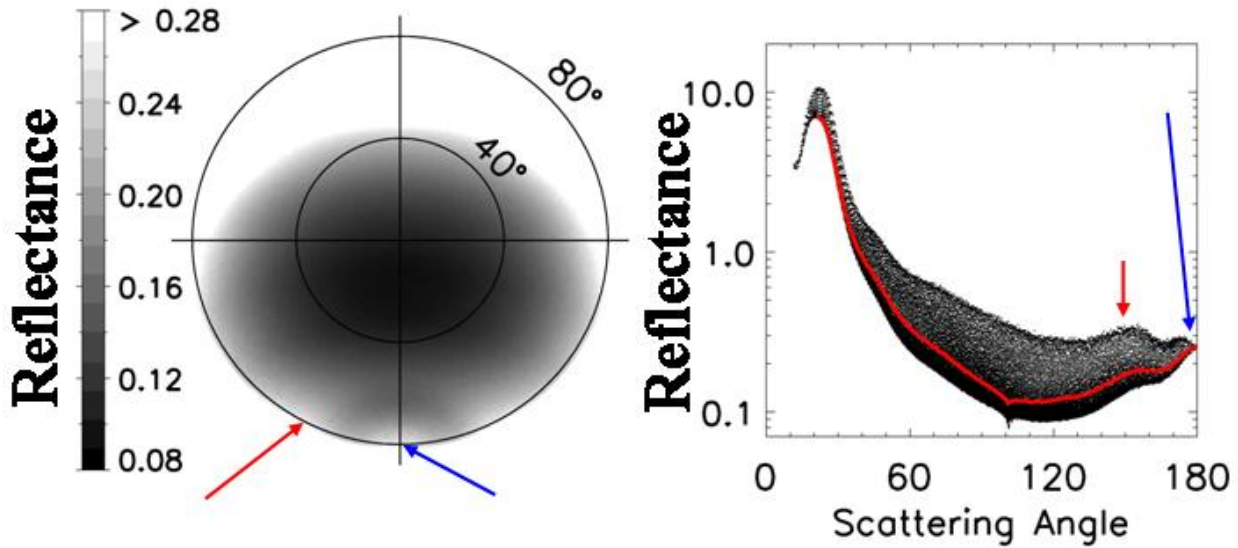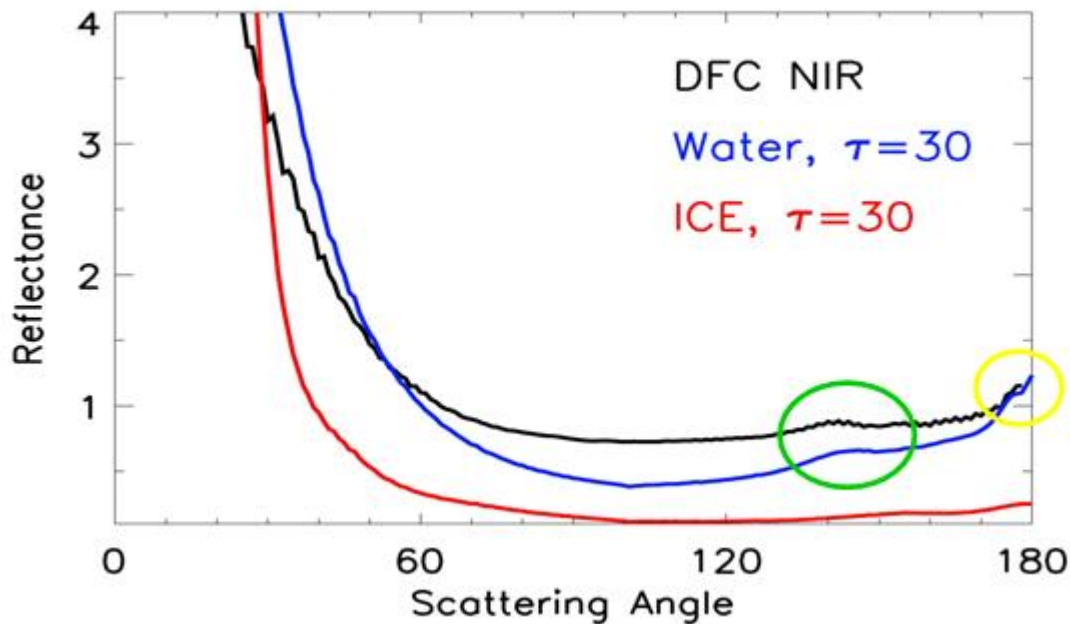**Figure 8**. Calculated reflectance fields for water clouds (τ=30) with effective radius of 12 μm.

Figure 9. Calculated reflectance fields for ice clouds consisting of ABRs (τ=30).

Figure 10. The mean reflectance of the DFC NIR and the calculated mean reflectance of water and ice clouds as a function of scattering angle.

Conclusions

The reflectance fields of relatively horizontally homogeneous mixed-phase boundary layer clouds were derived using DFC radiance measurements acquired during the 2004 M-PACE campaign. They were then compared with calculated reflectance fields of water and ice clouds using scattering phase functions of water droplets and aggregates of bullet rosettes. The most significant findings in this study are summarized as follows:

- DFC data can be used to determine the directional dependence of reflectance that can be compared with theoretical conclusions of the reflectance function for water and ice clouds.

- The 12 selected DFC scenes showed a cloudbow at the primary rainbow angle of 140° and backscattering, which are intrinsic scattering features of water clouds.

- Better agreement between the DFC and water cloud reflectance function than between the DFC and ice cloud reflectance function was noted, which is consistent with in-situ observations that show the tops of the M-PACE clouds were dominated by water.

Acknowledgments

Corresponding Author

Junshik Um, junum@atmos.uiuc.edu, (217)333-9056

References

Macke, A, R Dlhopolsky, J Mueller, R Stuhlmann, and E Raschke. 1995. "A study of bidirectional reflectance functions for broken cloud fields over ocean." *Advances in Space Research* 16:55-58

McFarquhar, GM, G Zhang, J Verlinde, M Poellot, A Heymsfield, and G Kok. 2005. "Assessing current parameterization of mixed-phase clouds using in situ profiles measured during the Mixed Phase Cloud Experiment." Extended Abstracts, Fifteenth ARM Science team meeting, Daytona Beach, Florida.

Um, J, and GM McFarquhar. 2006. "Single-scattering properties of aggregates of bullet rosettes in cirrus." *Journal of Applied Meteorology and Climatology*, In review.